

PGE 385K – Advanced Multi-Well Formation Evaluation

Homework Assignment #1: Shaly-Sandstone Interpretation

Misael Morales and Oriyomi Raheem

October 05, 2023

Executive Summary:

Petrophysical interpretation of laminated shaly-sandstone sequences is challenging but essential for accurate characterization of hydrocarbon energy resource systems, such as deltaic depositional environments or turbidite sequences. We perform a comprehensive analysis to estimate the properties of laminated shaly-sandstone sequence for its electrical, storage, and flow properties. The data is focused on the interval of 9,600 ft MD to 10,200 ft MD and contains both log and core measurements. Core images are also available to compare and validate our understanding of the petrophysical properties observed. The analysis is performed using Python, and we compare several techniques for the estimation of properties based on different petrophysical measurements. These included a linear estimation of the volumetric concentration of shale based on the Gamma Ray log, as well as a minimization routine to solve a system of equations from the parallel- and perpendicular-to-bedding-plane resistivity measurements. The analysis yielded an average fluid density of 0.4 g/cm^3 , in the interval of 9,730 ft to 9,825, namely the potential hydrocarbon-bearing zone. Further validation is done by analyzing the cross-plots of several formation properties and the Thomas-Steiber diagram. An analysis of the clay type is also performed to ensure that the shale laminae in the sandstone are representative of the top and bottom shales. In conclusion, we prepare a thorough workflow for the petrophysical interpretation of a laminated shaly-sandstone sequence and quantitatively and qualitatively estimate the electrical, storage, and flow properties of the formation.

1. Download the example LAS file and core data accompanying this homework project.
Plot the core data together with the well logs and depth-shift them if necessary.
Discard/flag measurements with dubious quality.
2. Consider the depth interval between 9,600 and 10,200 ft MD.

The data is loaded into Python using *lasio*. Figure 1 shows the triple-combo logs. We verify that the log and core data are corresponding in depth, and thus do not require depth shifting. Minor adjustments could potentially be made to completely align the log data, but the provided data appears to have been already depth-shifted. We crop the log data to be in the interval of [9,600 , 10,200] ft MD.

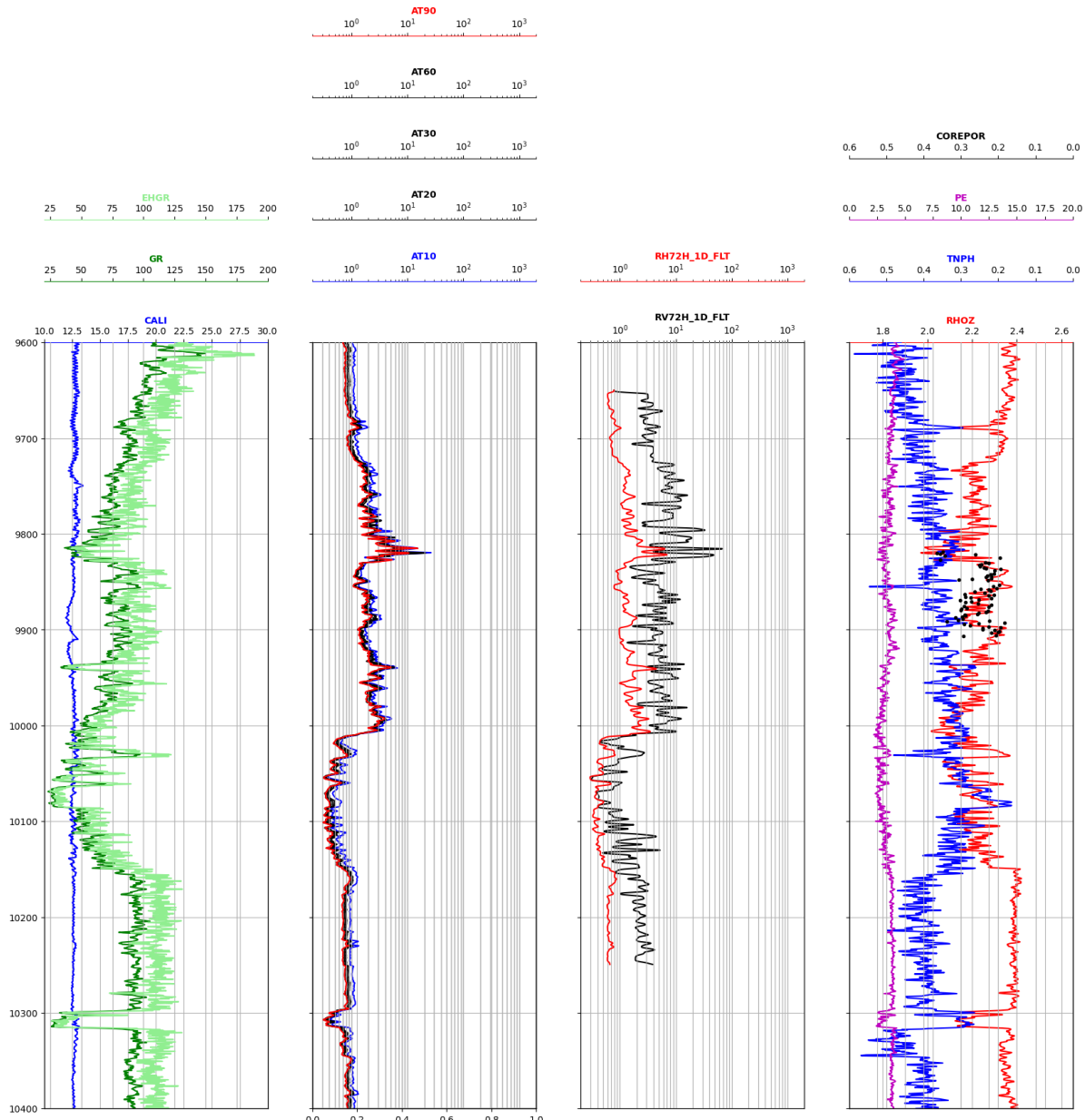


Figure 1: Triple-Combo visualization of log data.

There is a significant spike in the Gamma Ray (GR) log around 9610 ft. However, besides this dubious measurement, the majority of the log data appears to be conformal with the expected properties. We can qualitatively determine that this is a laminated shaly-sandstone sequence based on the high frequency variations in GR and the parallel- and perpendicular-to-bedding plane resistivity logs (R_V , R_H).

Looking at the caliper log, we observe that there are several places along the wellbore (e.g., 9730 ft, 9905 ft) where the whole appears to not be in-gauge. However, the measurements for the other logs appear to behave as expected, and most likely do not pose a major threat to the interpretation workflow.

Furthermore, by looking at the logs we can infer that this well was using oil-based mud (OBM). We observe a separation in the deep (AT90) and shallow (AT10) resistivity logs in the shales that is not quite present in the aquifer or potential hydrocarbon-bearing zone, and the AT10 measurements are consistently the largest value of resistivity along the entire wellbore, so OBM was used for the entirety of the well. Thus, we keep in mind that AT10 can be partially influenced by the effect of OBM, as well as spectral GR and photoelectric factor (PEF) logs.

3. Identify lithology, water zones, and possible hydrocarbon zones. Make use of cross-plots to guide your analysis. What possible type of outcrop and sedimentary sequence do the well logs and core photographs indicate?

We make the cross-plot of resistivity versus gamma ray, as shown in Figure 2, and highlight the water-bearing sands, hydrocarbon-bearing sands, and shale zones with blue, red, and green, respectively. These clusters are automatically obtained using a Gaussian Mixture Model with K-means++ initialization. Significant model validation and hyperparameter tuning had to be done to obtain a clustering consistent with our petrophysical (and visual) classification of the EHGR-vs-AT90 properties. We verify these three lithologic zones by plotting the PDF of EHGR by zone.

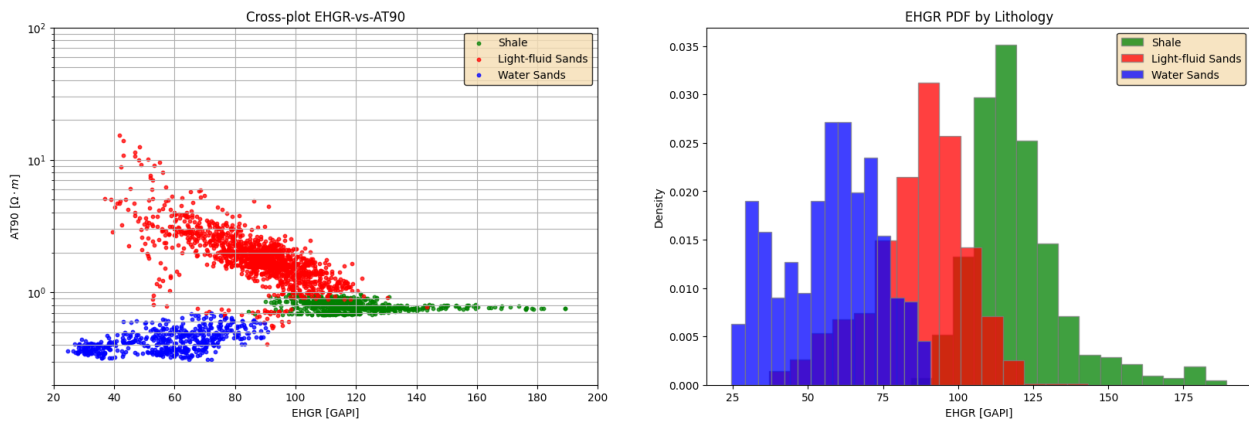


Figure 2: (left) Cross-plot for EHGR vs AT90, (right) PDF of EHGR by lithology.

Furthermore, we interpret the characteristics of the formations with respect to their high-resolution bulk density (RHO8) and their resistivity anisotropy with respect to PEF, as shown in

Figure 3. We observe that points in the water-bearing sands correspond to low resistivity points and higher bulk-density.

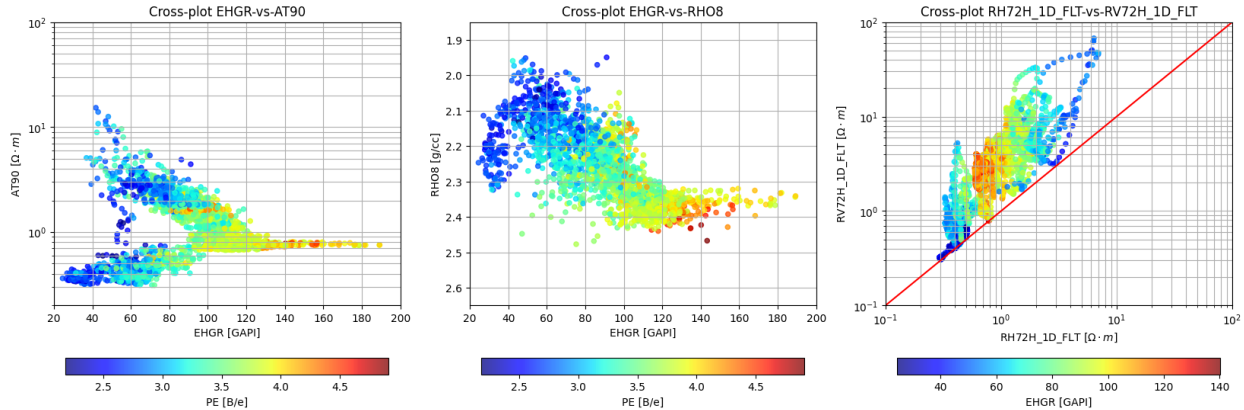


Figure 3: Cross-plots for EHGR-vs-Resistivity (left), EHGR-vs-Density (middle) and Resistivity Anisotropy (right).

It is important to note that there is clear anisotropy and lamination, as shown in Figure 3(b). The cross-plot of RH-vs-RV shows that the resistivities do not lie on the 45° line, as shown in Figure 3(c). In this low-resistivity pay (LRP) formation, the sands are interlayered sands with shale laminae and the effective resistivity can be resolved from the horizontal and vertical components.

Following this interpretation, and correlating to the core photographs from Figure 4, we can identify the water zones and possible hydrocarbon zones as shown in Figure 5. The green-shaded regions represent the shales, while the red-shaded region is the possible hydrocarbon zone and the blue-shaded region the water zone. The possible hydrocarbon zone can be found between 9,720' and 10,010', while the water zone can be found between 10,300' and 10,150'.

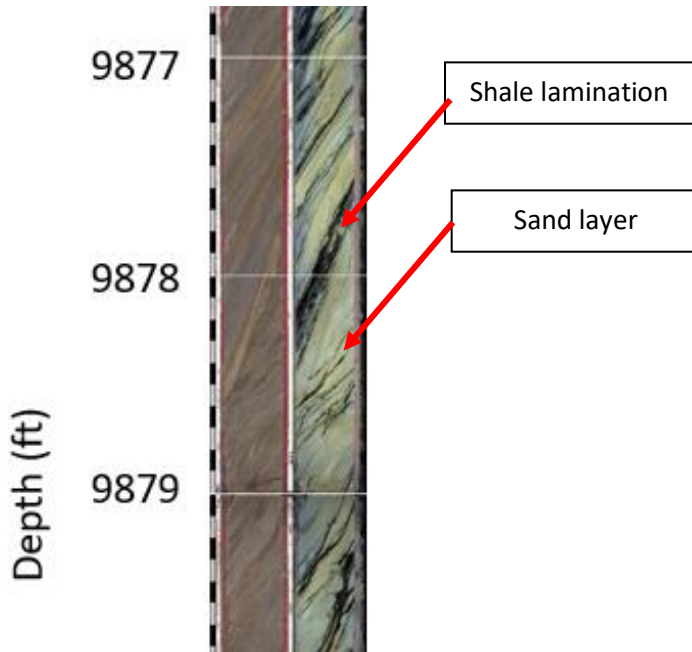


Figure 4: Core photograph from 9877' to 9880' showing clear shaly-sand laminations.

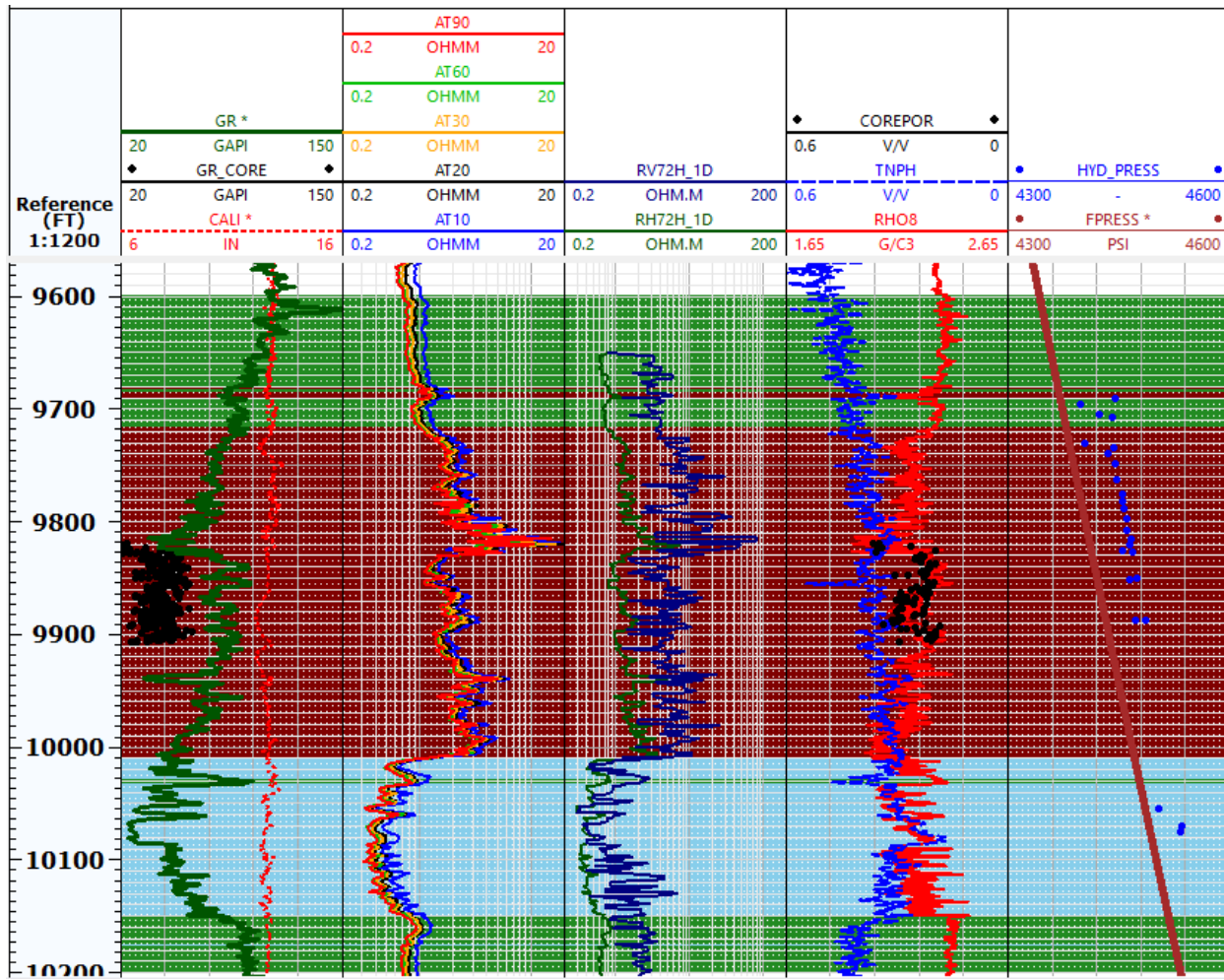


Figure 5: Interpretation of water zone and possible hydrocarbon zones from log and core data.

Despite identifying the water and hydrocarbon zones, we can also conclude that the sands bearing these two fluids are highly laminated, as mentioned with Figure 3(b). This can be inferred from the well logs including GR, TNPH and RHO8. Furthermore, the core photographs, as shown in Figure 4, show clear laminations of shale and sand. Therefore, the data for log and core measurements show a typical depositional environment for a deltaic sequence, with recursive transgressive and regression of the shoreline and deposition of sand- and silt-sized particles to form this shale-sand sequence. From Walther's Law of superposition, which states that sediments are deposited horizontally in sequence, we can infer that these inclinations in dip and azimuth are a result of post-depositional tectonic forces that caused uplift and folding of the layers. Thus, we now encounter a strongly-dipping laminated sequence of shaly-sand sediments.

It is also important to note that these laminations are not perfectly perpendicular to the well inclination, but instead pose a dipping angle with respect to the well. This is mostly likely due to post-depositional tectonic forces bending and uplifting the formation. Therefore, the horizontal and vertical resistivities actually represent perpendicular- and parallel-to-bedding plane anisotropy and not purely horizontal and vertical.

- 4. Verify that the gamma ray log truly responds to shale concentration. Estimate volumetric concentration of shale by two different methods. Diagnose whether shale distribution is laminar, dispersed (grain-coating clay), or structural. Identify “pure” shale segments in the well and verify that shale properties remain constant with depth within the sedimentary sequence. Identify formation tops for analysis/calculations if deemed necessary.**

We observe two main shale zones in the interval of interest. These are located directly above the possible hydrocarbon zone, and directly below the water zone, at approximately 9600-9720' and 10150-10400', respectively. These are confirmed with the triple combo log from Figs 1 and 4.

We can also verify that the top and bottom shales have similar properties by examining cross-plots. Figure 6 shows the cross-plots of POTA-vs-HTHO, RHO8-vs-TNPH, and EHGR-vs-RHO8, and highlight the top and bottom shales. These interpretation shows that both shales have similar properties and composition, therefore it is safe to assume that a pure shale is representative of the laminations in the entire formation and can be used for a simplistic evaluation of the petrophysical properties.

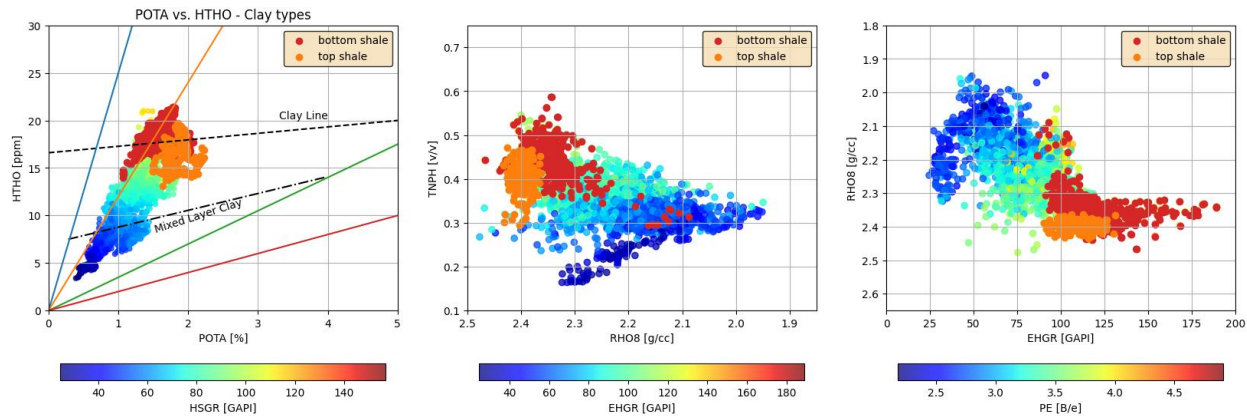


Figure 6: Cross-plots for Top and Bottom Shale

It can be observed that the vertical resistivity in the reservoir shale laminae are closer to those of the top shale, though similar to both top and bottom. However, we will guide our estimation of the “pure” shale properties using the top shale properties. We estimate the volumetric concentration of shale, C_{sh} , as follows:

$$C_{sh} = \frac{\gamma - \gamma_s}{\gamma_{sh} - \gamma_s} \quad (1)$$

where the following points are used to identify the sand and shale points:

Table 1: Shale and Sand properties for C_{sh} and shale corrections

	Depth [ft]	EHGR [GAPI]	PHI-D [v/v]	PHI-N [v/v]	ρ [g/cc]
Shale point	9,651.0	140.2567	0.1861	0.4640	2.3340
Sand point	10,068.5	24.5519		-	

This traditional technique for the estimation of C_{sh} will be denominated as the “linear” estimation method for the rest of our workflow.

The second way to calculate C_{sh} is by solving the system of equations for R_H and R_V given by:

$$\begin{cases} R_V = C_{sh}R_V^{sh} + (1 - C_{sh})R_S \\ \frac{1}{R_H} = \frac{C_{sh}}{R_V^{sh}} + \frac{1 - C_{sh}}{R_S} \end{cases} \quad (2)$$

This yields a system of 2 equations and 2 unknowns, namely C_{sh} and R_S . The values of R_H^{sh} and R_V^{sh} can be obtained from the parallel- and perpendicular-to-bedding-plane resistivity logs at the pure shale point, and found to be 0.7746 and 2.8133, respectively. This system of equations is solved at each depth using a constrained minimization solver, `scipy.optimize.minimize`, with a bound on $C_{sh} \in [0,1]$ and the L-BFGS-B method (limited memory BFGS with bounds), as shown in Figure 7a. The objective function is the ℓ_2 -regularized least-squares solution of the system of equations to ensure that the values of C_{sh} and R_S do not overshoot significantly.

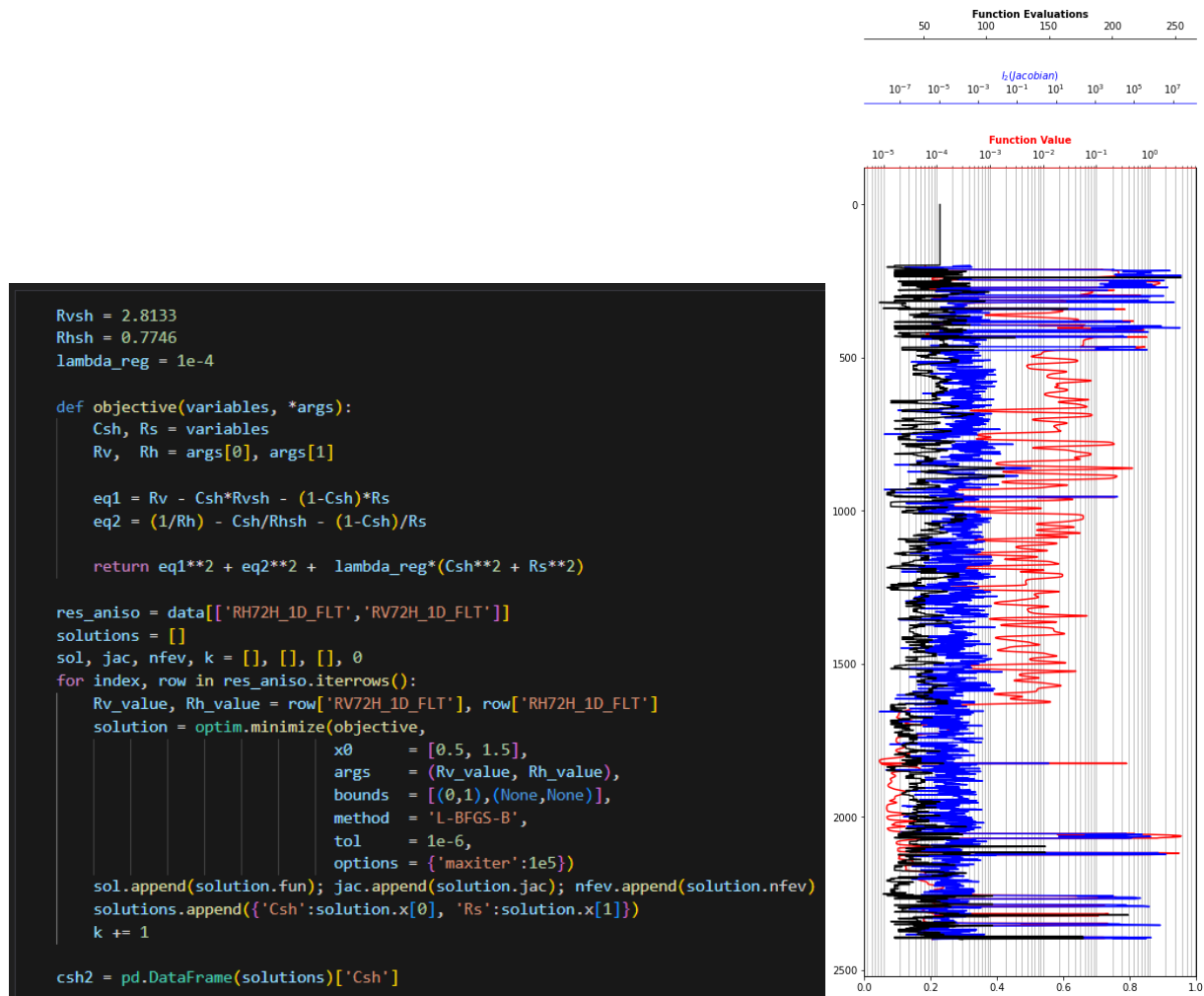


Figure 7: (left) Minimization routine to solve the system of parallel- and perpendicular-to-bedding-plane resistivities. (Right) Objective function value, l_2 (Jacobian) and number of function evaluations at each depth point for the solver.

The minimization procedure goes depth-by-depth and calculates the C_{sh} and R_s values. At each depth, we iterate the L-BFGS-B minimizer until convergence of the objection function, namely:

$$\begin{aligned} \min_x & \|f_1(x) + f_2(x)\|_2^2 + \|x\|_2^2 \\ \text{s.t. } & 0 \leq C_{sh} \leq 1 \end{aligned} \quad (3)$$

Where x is the parameter vector given by $x = [C_{sh} \ R_s]^T$ and f_1 and f_2 represent the equations in the system for parallel- and perpendicular-to-bedding-plane resistivity.

The black curve on Figure 7b shows the number of function evaluations at each depth and reflects the higher difficulty of estimated C_{sh} in the shale lamination layers. The red and blue curves display the function value and the ℓ_2 -norm of the Jacobian at each depth, respectively. We see that the Jacobian is ill-behaved in the top and bottom shales, but stable within the main/central portion of the well. Thus, we believe we can trust the results of this inversion method and proceed with our petrophysical evaluation using this $C_{sh}^{(V|H)}$.

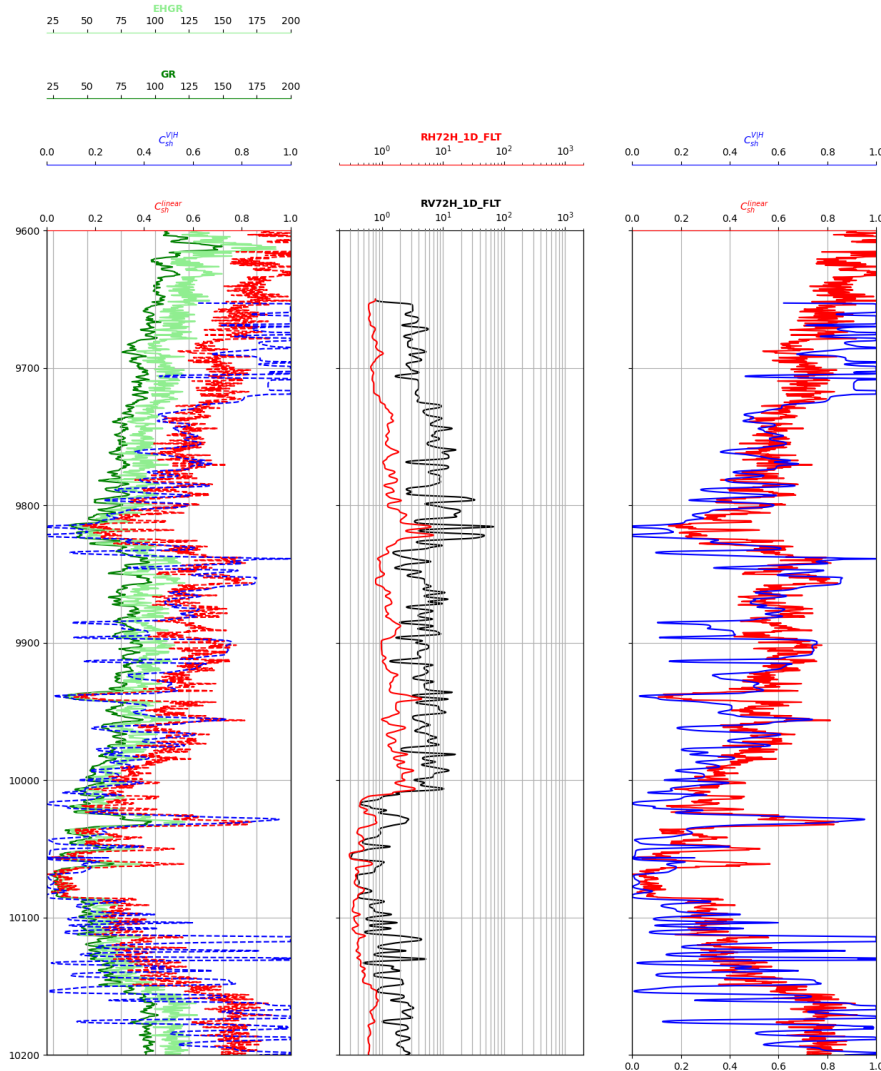


Figure 8: Comparison of C_{sh} estimation from linear technique and minimization routine

Figure 8 shows C_{sh} as a function of depth. The right-most track is a comparison of the C_{sh} obtained from the linearization technique (C_{sh}^{linear}) against the estimation obtained by the minimization routine ($C_{sh}^{V|H}$). The left-most track superimposes the two C_{sh} estimations with the GR log, and the center track shows the R_H and R_V values. First, we observe that the minimization routine only calculates C_{sh} on the interval where we have $\{R_H, R_V\}$, and tends to overshoot to 0 and 1 in “pure” shales and “pure” sands. The linear estimation of C_{sh} is more consistent with the GR log but can be hard to differentiate the laminations present in the formation.

5. Calculate sandstone porosity and fluid density. Compare the calculated porosities to core data, pore pressure gradients, ~~and sonic porosities~~. Note that this item is related to the items below.
6. Using the parallel- and perpendicular-to-bedding-plane resistivities, calculate hydrocarbon pore volume as a function of depth using the interpretation procedure intended for shale-laminated sandstone. Assume that $a = 1.0$, $m = 2.1$, and $n = 1.9$ in sandstones. Calculate hydrocarbon density and compare your calculations to fluid density interpreted from pore-pressure gradients.

To obtain the corrected sandstone porosity and fluid density considering C_{sh} , we use the following:

$$\begin{cases} \phi_N^{corr} = \frac{\phi_N - C_{sh}\phi_N^{sh}}{1 - C_{sh}} \\ \phi_D^{corr} = \frac{\phi_D - C_{sh}\phi_D^{sh}}{1 - C_{sh}} \end{cases} \quad (4)$$

We assign the “pure” shale density and neutron porosity to be 0.1861 and 0.4640, respectively, following our results from Table 1. The first step is to correct ϕ_N to sandstone units. Next, we apply the correction from Eq. 4 to account for the impact of shale and obtain the corrected porosities. This is given by Eq 5, and the total porosity is computed using Eq 6.

$$\phi_s = \frac{\sqrt{\phi_N^{corr2} + \phi_D^{corr2}}}{2} \quad (5)$$

$$\phi_T = (1 - C_{sh})\phi_s + C_{sh}\phi_D^{sh} \quad (6)$$

The estimated porosity is shown in Figure 9. We compare the performance of both methods to estimate C_{sh} and their prediction of ϕ_s and ϕ_T . Overall, we see reasonable agreement for the total porosity, ϕ_T , using either the linear estimation for of C_{sh} or the optimization routine. Figure

10 is the Thomas-Steiber diagram to confirm that C_{sh} and ϕ_T agree and belong to a similar class. Toward very high C_{sh} , we observe a dispersion in the results. This corresponds to the fact that in potential hydrocarbon-bearing zones we might observe a different effect in the estimated porosity versus volumetric concentration of shale, and to the fact that we might still have shaly-sandstone laminations, but the properties of these laminations are not exactly the same with each other.

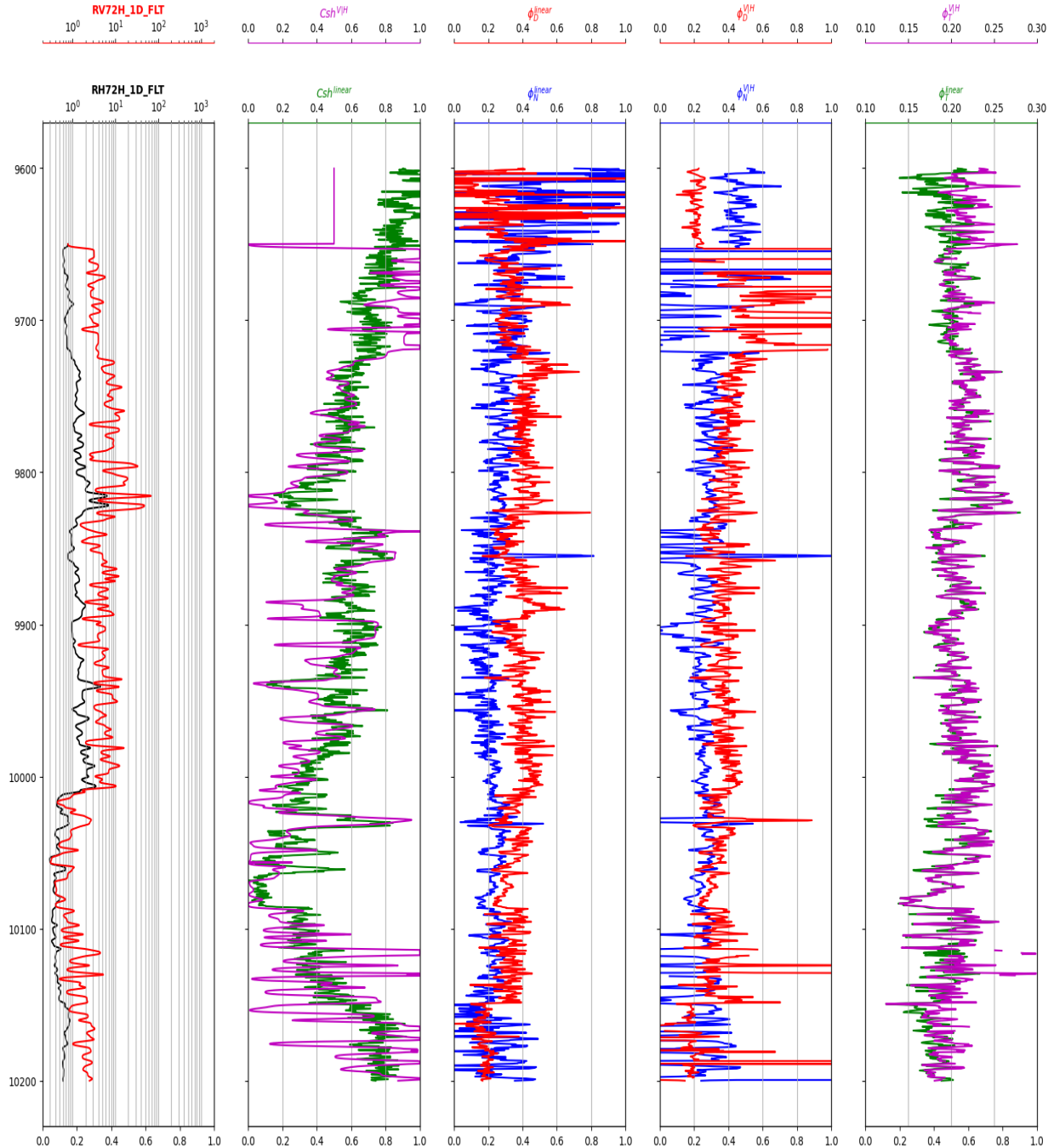


Figure 9: Estimation of ϕ_T using both C_{sh} estimation techniques (green is linear, magenta is optimization).

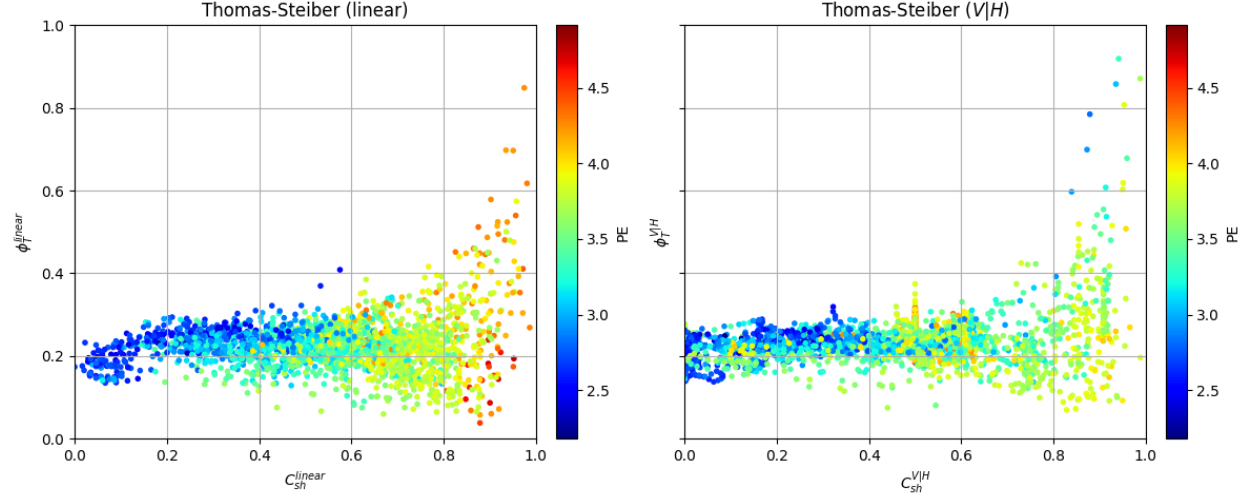


Figure 10: Thomas-Steiber Diagram using the linear and minimization-based procedures.

We also verify our results to the core data and pore pressure gradients, as shown in Figures 11 and 12. We observe that the estimated ϕ_T is close to the COREPOR values, since our ϕ_T estimates are most accurate in the sand layer and tend to deviate in the shale layers.

Figure 12 shows the estimated porosity values against the pore pressure gradients as well as core data. This is windowed around the sand layer, where the core samples are taken, to increase the resolution and qualitatively compare the match between estimated porosity and core values.

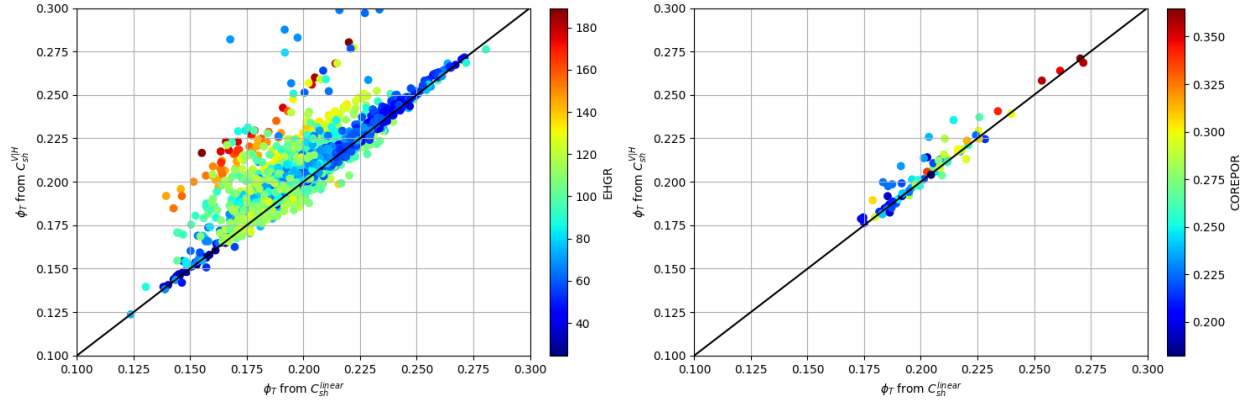


Figure 11: Comparison of estimated ϕ_T with COREPOR

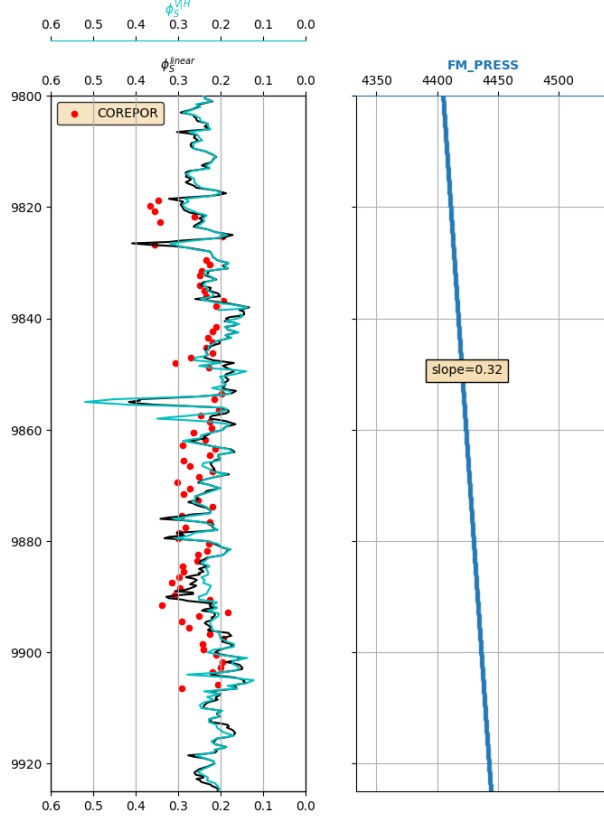


Figure 12: Estimated ϕ_S with COREPOR values and pore pressure gradient estimation.

At the clean sandstone aquifer ($\sim 10068.5'$), the formation resistivity is approximately $0.3619 \Omega m$. Using the traditional form of Archie's equation with the given parameters $\{a, m, n\} = \{1.0, 2.1, 1.9\}$, we obtain the following R_W :

$$R_S^{10068.5} = \frac{R_W^{10068.5}}{\phi_S^{2.1}} \Rightarrow R_W = \phi_S^{2.1} R_S \rightarrow R_W = 0.02 \Omega m$$

We then correct the resistivity as a function of depth using the volumetric concentration of shale. At the shale layers, we have a formation resistivity given by:

$$\frac{1}{R_t} = \frac{C_{sh}}{R_{sh}} + \frac{1 - C_{sh}}{R_S} \Rightarrow R_S = \frac{1 - C_{sh}}{\frac{1}{R_t} - \frac{C_{sh}}{R_{sh}}} \quad (7)$$

The water saturation is then given by:

$$S_W = \left(\frac{R_W}{R_S \phi_S^{2.1}} \right)^{\frac{1}{1.9}} \quad (8)$$

This is further confirmed by using a Pickett plot of log-resistivity against log-porosity and Buckles plot for S_w against porosity, as shown in Figure 13. The water saturation values obtained are shown in Figure 13.

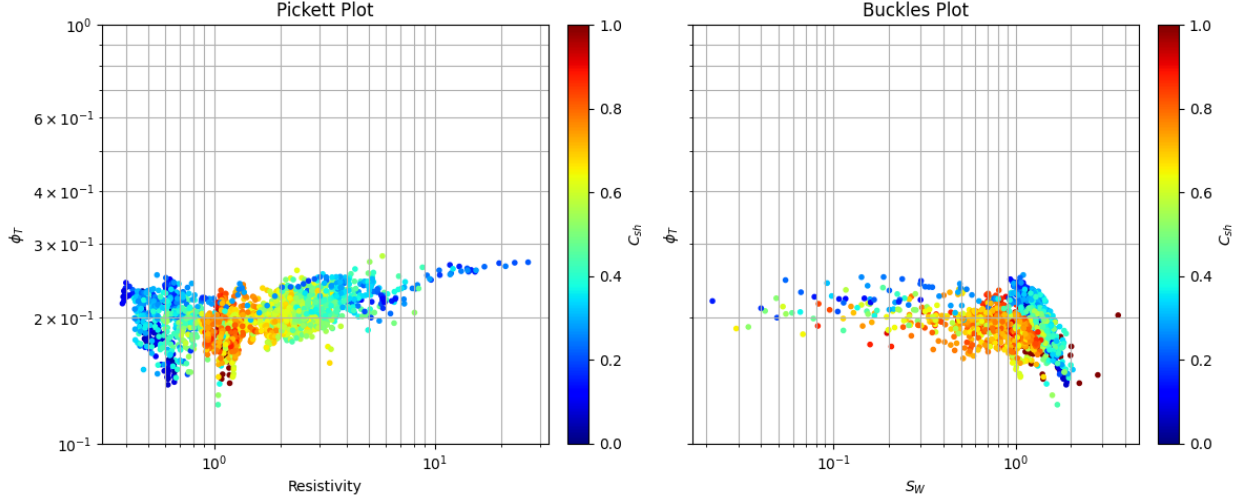


Figure 13: (left) Pickett Plot (right) Buckles Plot

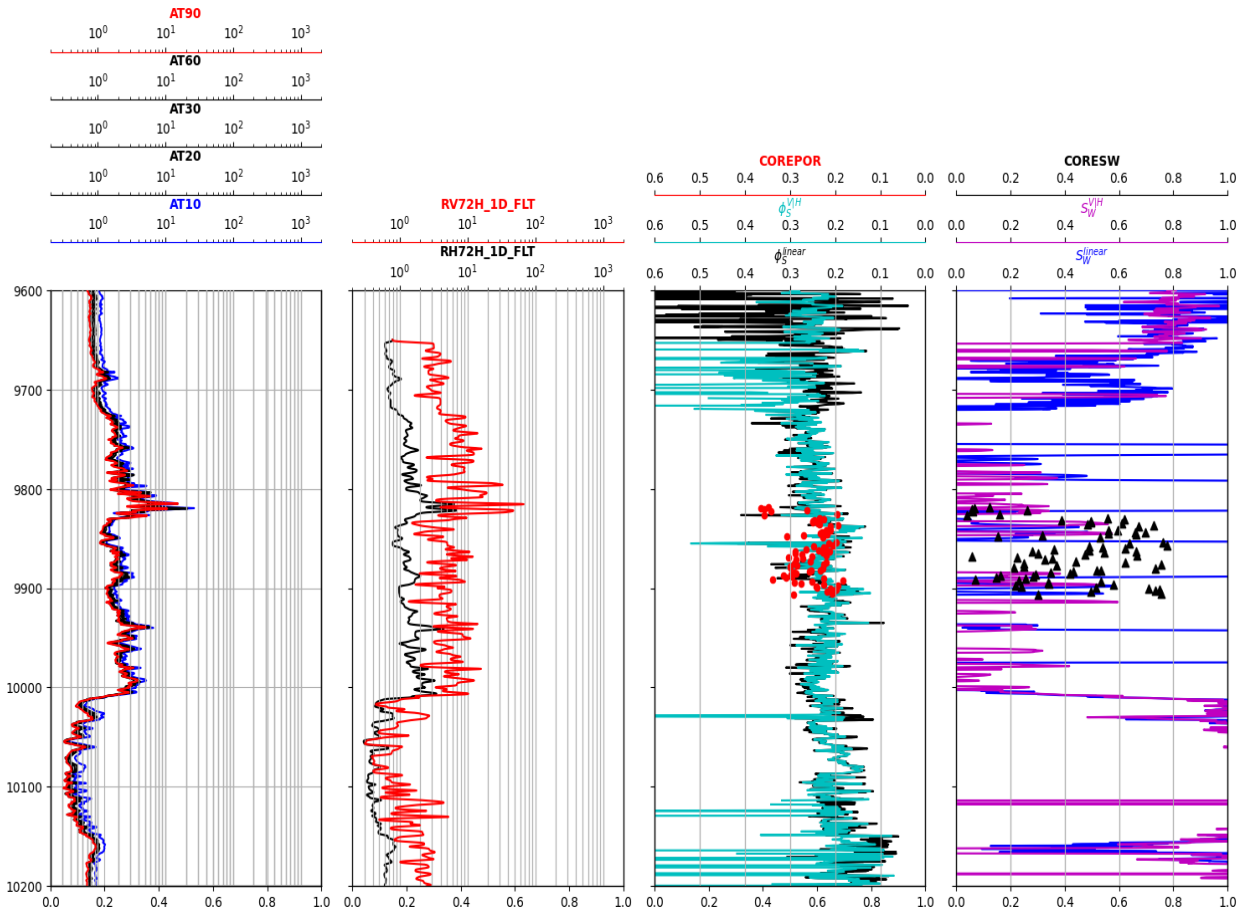


Figure 14: Water Saturation estimation using linear and optimization-based C_{sh} .

Fluid density is calculated using the following derivation:

$$\rho_b = \rho_f(1 - C_{sh})\phi_s + \rho_s(1 - C_{sh})(1 - \phi_s) + \rho_{sh}C_{sh}$$

$$\rho_f = \frac{\rho_b - 2.65(1 - C_{sh})(1 - \phi_s) - 2.3509C_{sh}}{(1 - C_{sh})\phi_s}$$

Figure 14 shows the fluid density log obtained with the two methods for calculating C_{sh} .

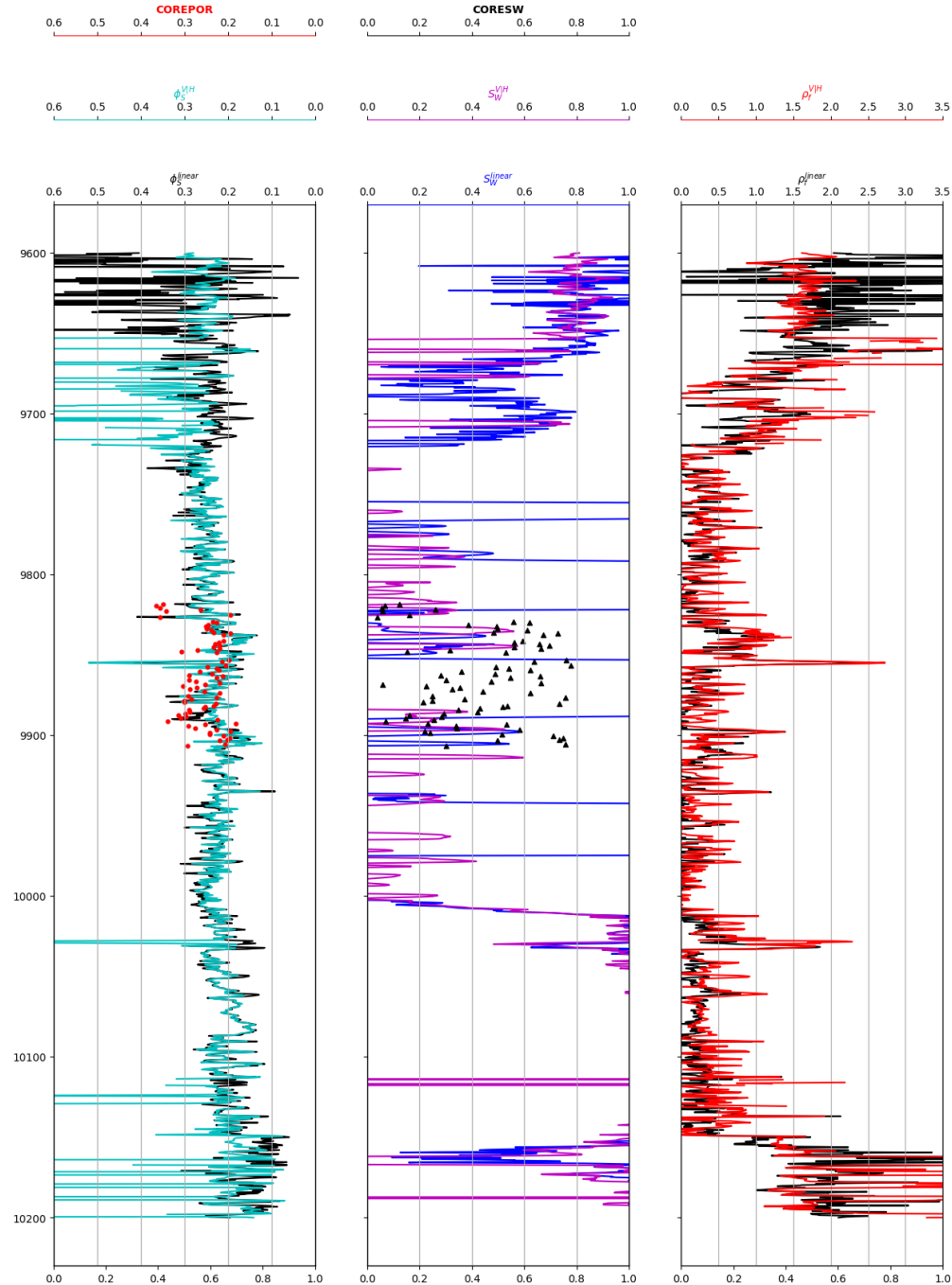


Figure 14: Fluid density log using linear and optimization-based C_{sh} .

7. Calculate S_{xo} . Verify that your calculations of S_w and S_{xo} are consistent with your calculation of sandstone porosity.

To calculate the saturation of the flushed zone, we use the shallow resistivity log at 10068.5' MD and obtain a reading of approximately $0.4989 \Omega m$. Then, we can calculate the flushed zone resistivity and saturation using Archie's equation as follows:

$$R_{xo} = R_{mf} \frac{a}{\phi^m} \frac{1}{S_w^n} \quad (9)$$

This simplification is done since we are in a well drilled using OBM and we can infer that the mud filtrate resistivity is that of the water resistivity where the saturation of water is exactly 1.

However, we must correct for the shaly-sandstone laminations in our sequence. For this, we apply the following procedure:

First, let R_{10} represent the shallow resistivity from the AT10 log. Then we have that

$$\frac{1}{R_{10}} = \frac{C_{sh}}{R_{sh}} + \frac{1 - C_{sh}}{R_{xo}} \quad (10)$$

We can then solve for R_{xo} at each depth since we have log measurements for R_{10} , and log estimates of C_{sh} and the shale-point resistivity R_{sh} .

The derivation leads to:

$$R_{xo} = \frac{R_{sh}R_{10}(1 - C_{sh})}{R_{sh} - R_{10}R_{sh}} \quad (11)$$

With this correction, we obtain the following values for R_{xo} in the fully water-saturated zone: $R_{xo} = 0.027 \Omega m$.

Without the shaly-sandstone laminated correction, we would have a simplified estimation of S_{xo} as follows:

$$S_{xo} = \left(\frac{R_{xo}}{R_S \phi_S^{2.1}} \right)^{\frac{1}{1.9}} \quad (12)$$

However, by applying the shaly-sandstone laminated correction to the resistivity values to obtain the saturation, in the potential hydrocarbon-bearing zone we can apply the corrected Archie's equation as a function of water saturation to obtain:

$$S_{xo} = \left[\frac{(R_{sh} - R_{10}R_{sh})R_w a}{\phi^m (R_{sh}R_{10}(1 - C_{sh}))} \right]^{\frac{1}{n}} \quad (13)$$

Recall $\{a, m, n\} = \{1.0, 2.1, 1.9\}$. We check this calculation on the aquifer zone to verify the results. Furthermore, we verify that the caliper log is in-gauge and there are no extraneous effects of the mud on the formation.

We obtain the following representative log for the flushed-zone saturation, shown in Figure 15. The logs for S_w and S_{xo} show very similar behavior but with mild differences or separations in specific areas, more notably in the potential hydrocarbon-bearing zone. This is a result of the fact that the well is drilled using OBM and therefore the resistivities in the flushed zone and the potential hydrocarbon-bearing zone will be affected by mud filtrate invasion and the relative displacement of fluids near the wellbore.

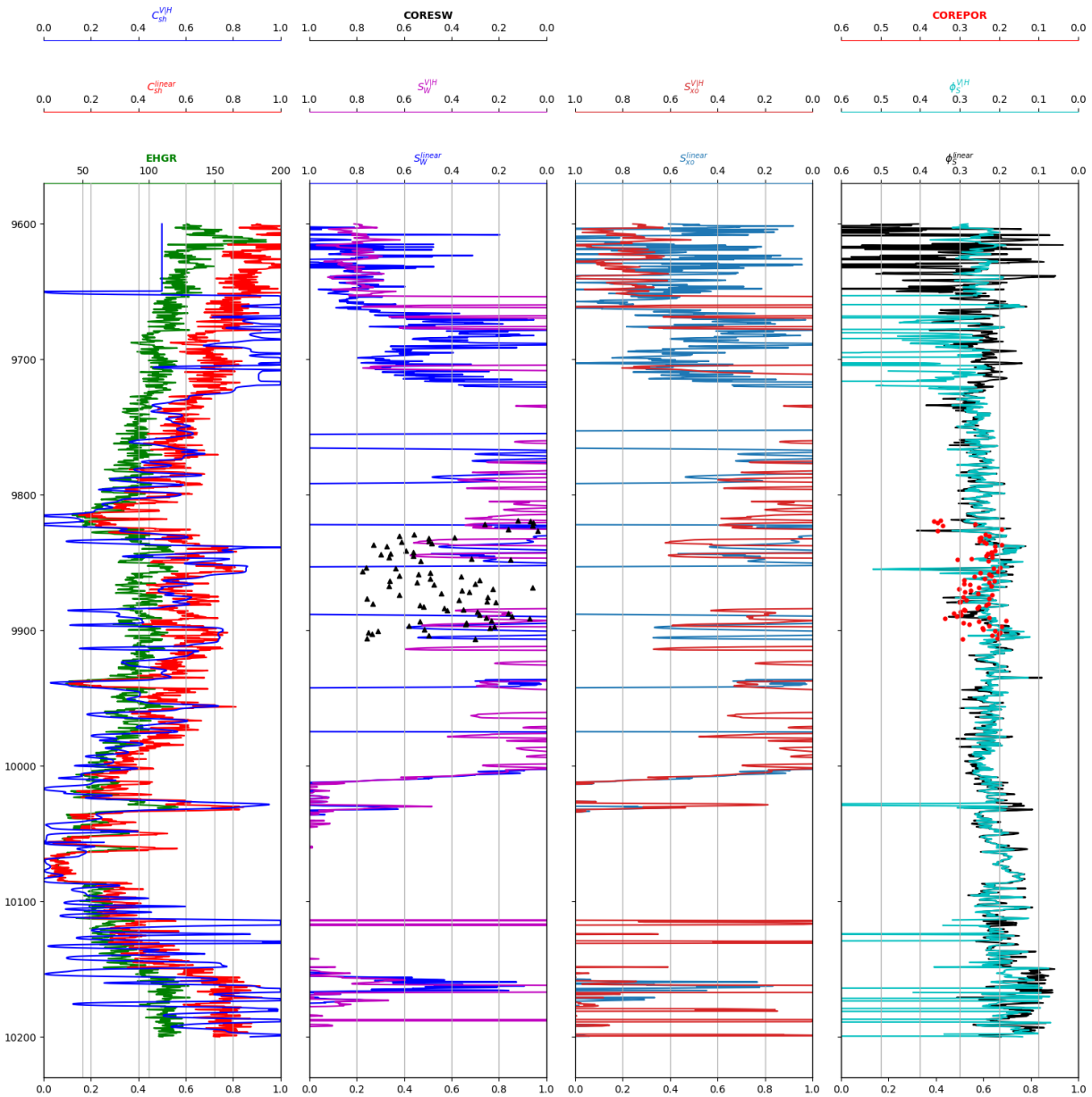


Figure 15: Calculated S_{xo} from linear and optimization-based C_{sh} .

8. Explore whether core permeability exhibits a clear correlation with your calculated sandstone porosities and irreducible water saturations.

There are several common equations to relate porosity to permeability. Using Wyllie-Rose's equation, we have that:

$$k = k_w \frac{\phi_s^\kappa}{0.25^\eta}$$

Where k_w is obtained from the aquifer zone and flushed-zone saturations. Similarly, we can look at Figure 16 and compare the lowest existing values of S_w .

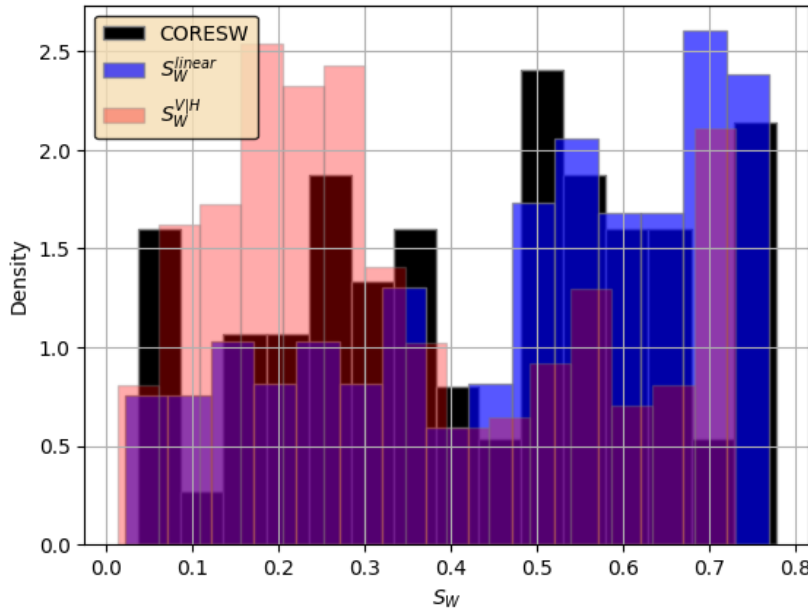


Figure 16: Distribution of S_w for core and log data.

We perform an initial guess with the typical parameters of $\{\kappa, \eta\} = \{7, 2\}$, but also go ahead and perform a least-squares minimization to obtain the best fit for permeability values given our porosity estimates. Figure 17 shows our estimated permeability logs.

It is important to note that the estimation of a (pseudo) permeability log from other measured formation properties is extremely approximate and inexact. Therefore, this should not be taken as ground truth and must be compared to core permeability measurements for verification. However, in Figure 17 we can clearly observe the shaly-sandstone laminations in the permeability response, and we can also identify the top and bottom shales, where the differences in shale and sandstone permeabilities are significant compared to those of the potential hydrocarbon-bearing zone which is assumed to be a more sand-dominated formation with thin shale laminae.

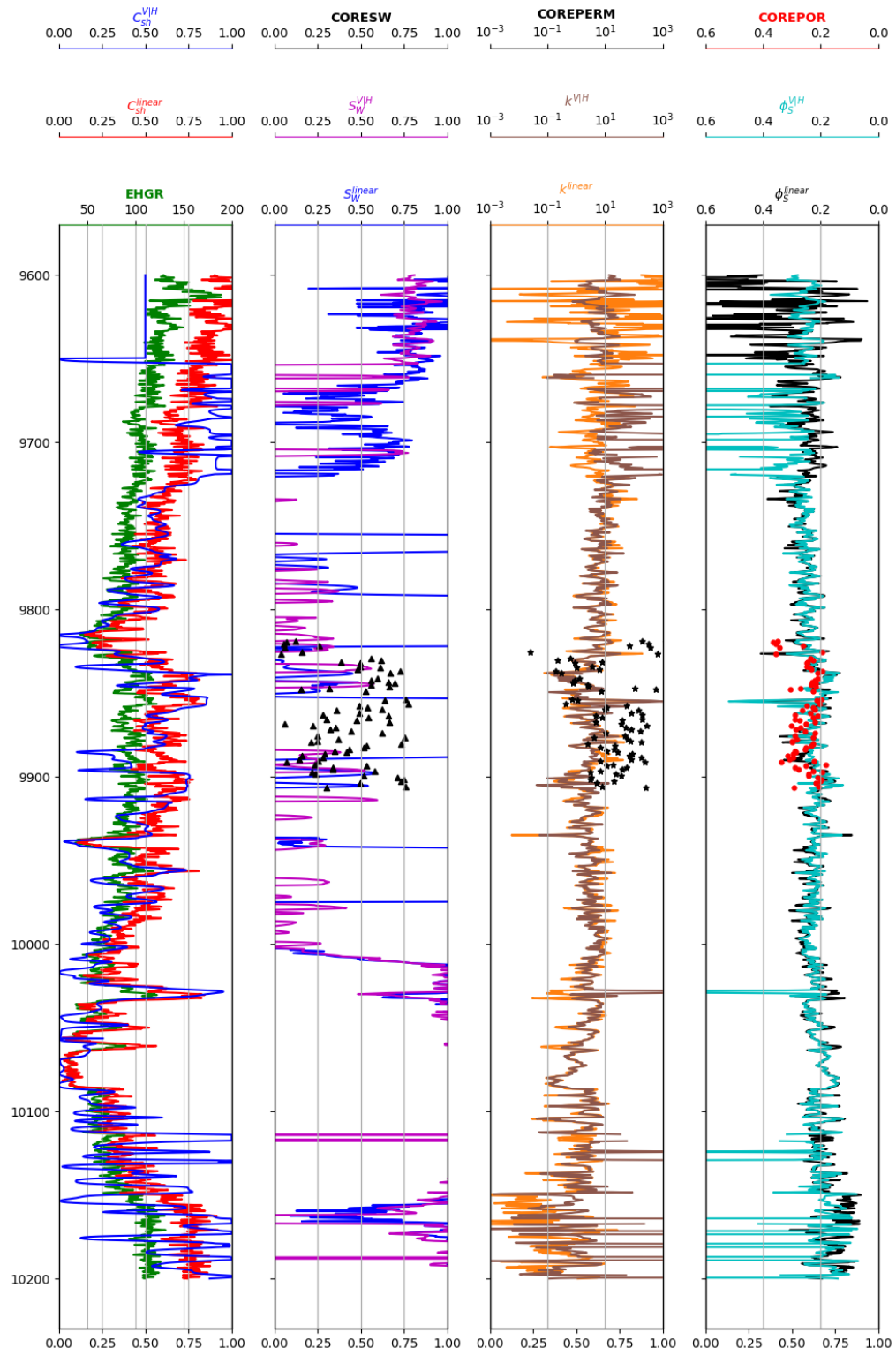


Figure 17: Estimated Permeability log from linear and optimization-based routines.

Next, we explore the relationships between the core permeability, estimated sandstone porosity and water saturation. Figure 18 shows that our predicted porosity values correspond appropriately with the relationship between the core porosity and permeability.

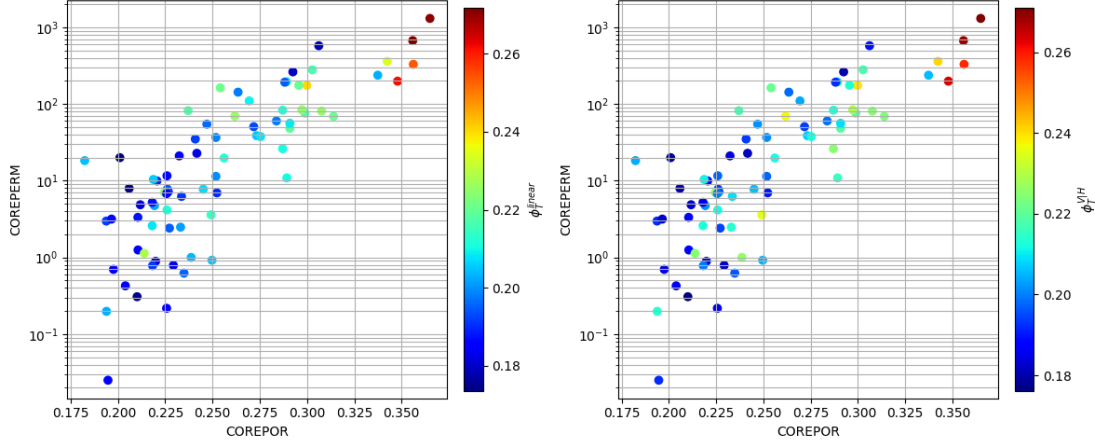


Figure 48: Core porosity and permeability against predicted porosity from linear and optimization-based C_{sh} .

Figure 19 shows that our predicted permeability is a bit underestimating the core permeability values; however, it shows good agreement between the core porosity, core permeability, and estimated permeability.

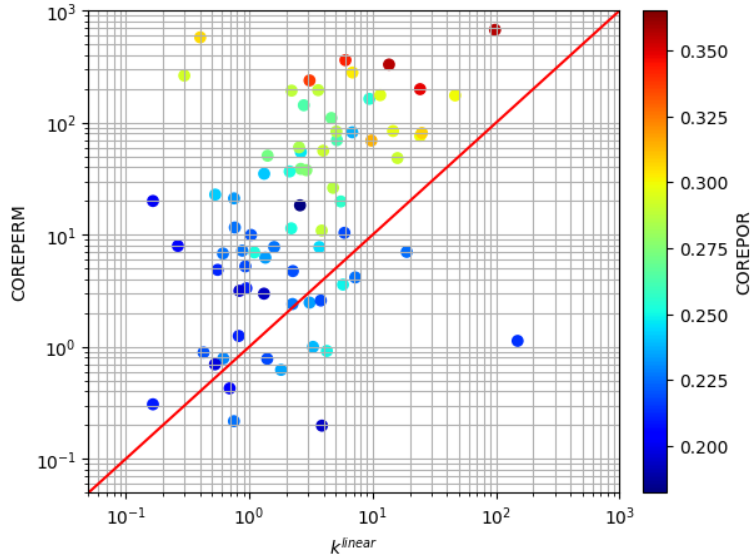


Figure 19: Comparison of COREPOR, COREPERM, and Estimated Permeability.

Next, we check the relationship between the core permeability and the flushed-zone saturation. Figure 20 shows a clear (negative) correlation between the core permeability and our estimated S_{xo} from both the linear and optimization-based estimation of C_{sh} .

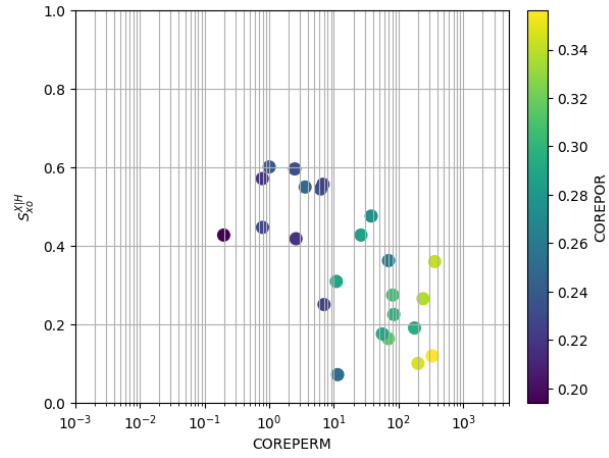


Figure 20: Core permeability again flushed-zone saturation.

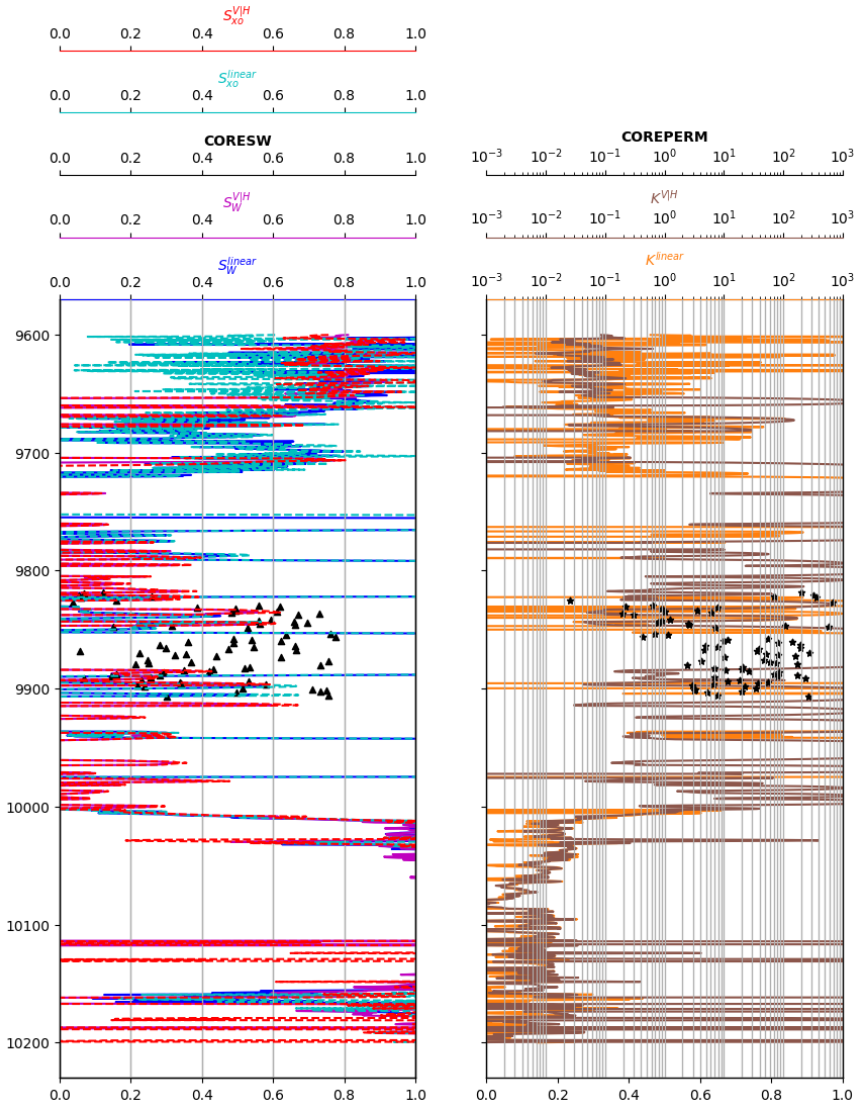


Figure 51: Comparison of core and log data for SW, SXO, and PERM